Article

Catalytic Decomposition of *n*-C$_7$ Asphaltenes Using Tungsten Oxides–Functionalized SiO$_2$ Nanoparticles in Steam/Air Atmospheres

Karen M. Cerón [1,2], Daniela Arias-Madrid [1], Jaime Gallego [3,*], Oscar E. Medina [1], Lidia E. Chinchilla [4], Farid B. Cortés [1] and Camilo A. Franco [1,*]

[1] Grupo de Investigación en Fenómenos de Superficie–Michael Polanyi, Facultad de Minas, Universidad Nacional de Colombia Sede-Medellín, Cra. 80 No. 65-223, Medellín 050034, Colombia; karen.ceron@correounivalle.edu.co (K.M.C.); daariasma@unal.edu.co (D.A.-M.); oemedinae@unal.edu.co (O.E.M.); fbcortes@unal.edu.co (F.B.C.)

[2] Laboratorio de Investigación en Catálisis y Procesos, Departamento de Química, Universidad del Valle, Cali 760001, Colombia

[3] Química de Recursos Energéticos y Medio Ambiente, Instituto de Química, Universidad de Antioquia UdeA, Calle 70 No. 52-21, Medellín 050010, Colombia

[4] Departamento de Ciencia de los Materiales, Ingeniería Metalúrgica y Química Inorgánica, Facultad de Ciencias, Universidad de Cádiz, Campus Río San Pedro, 11510 Puerto Real, Spain; lidia.chinchilla@uca.es

[*] Correspondence: andres.gallego@udea.edu.co (J.G.); caafrancoar@unal.edu.co (C.A.F.)

Abstract: A wide range of technologies are being developed to increase oil recovery, reserves, and perform in situ upgrading of heavy crude oils. In this study, supported tungsten oxide nanoparticles were synthesized, characterized, and evaluated for adsorption and catalytic performance during wet in situ combustion (6% of steam in the air, in volumetric fraction) of *n*-C$_7$ asphaltenes. Silica nanoparticles of 30 nm in diameter were synthesized using a sol–gel methodology and functionalized with tungsten oxides, using three different concentrations and calcination temperatures: 1%, 3%, 5% (mass fraction), and 350 °C, 450 °C, and 650 °C, respectively. Equilibrium batch adsorption experiments were carried out at 25 °C with model solutions of *n*-C$_7$ asphaltenes diluted in toluene at concentrations from 100 mg·L^{-1} to 2000 mg·L^{-1}, and catalytic wet in situ combustion of adsorbed heavy fractions was carried out by thermogravimetric analysis coupled to FT-IR. The results showed improvements of asphaltenes decomposition by the action of the tungsten oxide nanoparticles due to the reduction in the decomposition temperature of the asphaltenes up to 120 °C in comparison with the system in the absence of WO$_X$ nanoparticles. Those synthesis parameters, such as temperature and impregnation dosage, play an important role in the adsorptive and catalytic activity of the materials, due to the different WO$_X$–support interactions as were found through XPS. The mixture released during the catalyzed asphaltene decomposition in the wet air atmosphere reveals an increase in light hydrocarbons, methane, and hydrogen content. Hydrogen production was prioritized between 300 and 400 °C where, similarly, the reduction of CO, CH$_4$, and the increase in CO$_2$ content, associated with water–gas shift, and methane reforming reactions occur, respectively. The results show that these catalysts can be used either for in situ upgrading of crude oil, or any application where heavy fractions must be transformed.

Keywords: nanomaterials; catalysis; silica; asphaltenes; sodium tungstate; tungsten oxide; wet combustion

1. Introduction

The growth of the population, as well as the economic and technological developments, imply a continuous increase in the global demand for energy [1]. Consequently, unconventional crude oils, such as heavy crude oil (HO) and extra heavy crude oil (EHO),

among others, have gained significant importance [2–4]. These types of crude are characterized by high carbon–hydrogen ratios, and a lot of asphaltenes (2% to 20%, in mass fraction), high viscosity, and low American Petroleum Institute gravity (°API) [5].

Asphaltenes correspond to the fraction of the oil-soluble in aromatic hydrocarbons but are insoluble in alkanes [6]. Likewise, the asphaltenes contain plane polyaromatic hydrocarbons (PAH) with polar functional groups (mainly containing S, N, and O), metalloporphyrins of Ni and V, as well as aliphatic side chains [7–9]. The polycyclic nuclei are polarizable and are partially charged due mainly to the presence of heteroatoms, generating interactions of the types dipole–dipole, induced dipole–induced dipole, and π stacking [10]. In contrast, the aliphatic (peripheral) components avoid the proximity of the molecules because they generate steric hindrance [8,11–13]. The equilibrium between forces of attraction and repulsion gives rise to the tendency of aggregation in the asphaltenes, reaching to produce asphaltene aggregates of 5 nm–20 nm [14]. The pitfalls related to asphaltenes presence translate into higher economic expense and environmental impact [15]. Removing asphaltenes from crude oil would help to improve the crude oil quality and consequently reduce the costs of crude oil production and transportation, also generating a lower environmental impact [16]. Accordingly, several in situ technologies have been used for improving HO and EHO production to reduce the viscosity of the oil [17]. Procedures such as solvent injection, steam, and gas injection, as well as mechanical or thermal methods, are commonly used [14,18–22]. Among the thermal methods, wet in situ combustion is of interest as water is co-injected or alternately injected with the air to improve the heat consumption in the reservoir [23–26]. Wet in situ combustion is also called in situ steam generation or a combination of in situ combustion and waterflooding, where the heat is transferred to the oil bank front from the water injected [27]. During this process, different reactions occur simultaneously, generating physicochemical changes in the heavy oil, even leading to upgrading through viscosity reduction and API gravity increase. Nevertheless, the conversion of heavy and refractory fractions such as asphaltenes into lighter compounds struggles to occur behind the combustion zone, as the decomposition temperature could be higher than 400 °C [28–31].

The development of nanotechnology has allowed the oil and gas industry to be included among the broad applications of this phenomenon [32,33]. Adsorption of asphaltenes on different nanoparticles and the subsequent decomposition is considered as a viable and environmentally friendly solution for the development and recovery of HO and EHO [16,28,34–39]. Transition element oxides (TEO) provide a determinate characteristic that can be exploited to obtain selective adsorption of asphaltenes besides a better performance as catalysts for decomposition of them [39] and, at the same time, reducing problems associated with mobility, transport, production, and recovery [40,41]. Recently, supported and unsupported transition element oxide nanoparticles have been employed for asphaltene adsorption, and subsequently gasification [16,42–45], oxidation [28,36,46–50], and pyrolysis [35,51] as a new approach for the in situ upgrading of HO and EHO, providing useful information about effects of TEO and supported nanoparticles [16,35,36,46,52]. It is necessary to keep in mind that solid acid catalysts based on nickel or tungsten oxides clusters have shown to be active for dehydrogenation, isomerization, reforming, cracking, alcoholic dehydration, and olefin oligomerization reactions [52], in addition to the removal of sulfur and nitrogen atoms [53] correlated to the cracking reactions. On the other hand, the catalytic properties of a material are strongly related to their composition and the surface structure, which, in turn, can be determined by the conditions of synthesis [54,55], obtaining variations in the surface area, dispersion of the active phase, the resistance of acid sites, and effectiveness and selectivity in oxidative catalysis [55,56].

However, to the best of our knowledge, there are no studies related to the use of nanocatalysts in a wet in situ combustion atmosphere. Hence, this study employed, for the first time, nanomaterials based on tungsten oxides supported over silica nanoparticles and evaluated the effect of variations on synthesis method, such as the concentration of active phase precursor and calcination temperature, over the performance of the nanoparticles

for adsorption and catalytic decomposition of asphaltenes in wet in situ combustion atmosphere. In this sense, the synthesis was evaluated using incipient wetness technique, using three different concentrations and calcination temperatures: 1%, 3%, and 5% (mass fraction), and 350 °C, 450 °C, and 650 °C, respectively. The nanomaterials were physical, and chemically characterized by surface area (S_{BET}), dynamic light scattering technique (DLS), X-ray photoelectron spectroscopy (XPS), and H_2 pulse chemisorption. The adsorption was conducted in batch–mode experiments at 25 °C and the wet combustion decomposition was carried out by thermogravimetric analysis coupled to a mass spectrometer.

2. Experimental Section

2.1. Materials

Silica nanoparticles used in this study were synthesized using HCl, hexadecyltrimethylammonium bromide (98.0%, Panreac, Spain), deionized water, and sodium silicate (Protokimica, Colombia) as a precursor. $Na_2WO_4 \cdot 2H_2O$ and $(NH_4)_{10}H_2(WO_7)_6$ (Sigma-Aldrich, St. Louis, MO, USA) were used for the functionalization of nanoparticles. *N*-heptane (99%, Sigma-Aldrich, St. Louis, MO, USA) and toluene (99.5%, Merck GaG, Germany) were used for asphaltene isolation from crude oil and as a solvent on heavy oil model solutions, respectively.

2.2. Methods

2.2.1. Asphaltene Isolation and Characterization

Asphaltenes were isolated from a heavy crude oil (6.4° API) with an approximately contain asphaltenes of 13% (mass fraction), obtained from a reservoir located in southeast Colombia. Asphaltenes were extracted from the heavy crude oil sample by mixing each crude oil in a 40:1 ratio with *n*-heptane following the ASTM D2892 and ASTM D5236 [57–59]. An excess of *n*-heptane was added to the crude oil in a volume ratio of 1:40 (g·mL^{-1}). The mixture was then sonicated for 2 h at 25 °C and further stirred at 300 rpm for 20 h; then it was centrifuged for 30 min at 4500 rpm. The precipitated asphaltenes were filtered and washed with *n*-heptane until obtaining a shiny black tone. Details of the chemical and physical properties of the asphaltenes can be found in previous work [29].

2.2.2. Nanoparticles Preparation

The synthesis method used for obtaining SiO_2 nanoparticles was developed in previous works [60,61]. Some modifications to the protocol were made with the purpose of obtaining particle sizes that adjust to the IUPAC definition of nanoparticle (1 nm–100 nm) [62]. The procedure consists of the preparation of a silica suspension from an aqueous solution of sodium silicate (24.5% volumetric fraction, silicate/water) by the addition of hydrochloric acid (1 M) through the precipitation method under constant stirring. A sodium silicate solution (SSS) was prepared and heated until adjusting the temperature to 55 °C; using a constant stirring speed of 300 rpm, cetyltrimethylammonium bromide was dissolved until obtaining a concentration of 10% (in volumetric fraction) with respect to the SSS, then, a HCl solution was slowly added. The use of the acid had two purposes: first, to initiate the formation of a gel (pH: 9–9.5); and the second one was to acidify the solution and bring it to a pH of 1–1.5. Between two steps, the solution was stirred for 10 min, with no further addition of HCl, to prevent the formation of a strong silica gel. Then, the gel was aged for 20 h at 55 °C, and the nanoparticles obtained were washed using ethanol. Finally, the silica nanoparticles were dried for 8 h at 120 °C and calcined at 550 °C.

2.2.3. Surface Functionalization

Silica nanoparticles were dried at 120 °C. Sodium tungstate dihydrate $Na_2WO_4 \cdot 2H_2O$ and ammonium tungstate $(NH_4)_{10}H_2(W_2O_7)_6$ were used. The precursors were dissolved in a volume of water equal to the pore volume of a determined amount of the catalyst support. To determine volume of liquid required, the selected solid silica is dried at room temperature for several weeks, weighed, and immersed in alcohol for 20 min The

bubbling observed on the surface of the silica indicates that trapped air is being released. Once saturated, the silica is placed on an alcohol-saturated paper towel and immediately weighed at room temperature (20 °C). This process is completed in less than 10 s. The internal volume of the silica is calculated by converting the difference in masses of the alcohol-saturated silica and the dry aggregate to volume using the density of the alcohol.

The impregnation procedure in the support was carried out using incipient wet impregnation, which was carried out by adding, drop by drop, the precursor solution to the support until saturation.

Then, the impregnated materials were then dried at 120 °C for six hours, followed by calcination [28,37]. The calcination temperature was varied at 350 °C, 450 °C, and 650 °C separately for 4 h, obtaining the tungsten oxide nanoparticles. The hybrid or supported hygroscopic salt (called SHS) in this study was named using the chemical symbol of the support (i.e., Si) followed by the symbol of tungsten (i.e., W). If the precursor salt was the sodium tungstate dihydrate, the Na symbol was added after W. Then, it was included in the mass fraction percentage of the nominal tungsten used [28]. The number after the space indicates the calcination temperature of the material. For example, the sample SiWNa1 350 corresponds to nanosilica doped with 1% (in mass fraction) of sodium tungstate dihydrate and calcined at 350 °C. Table 1 lists the characteristics of the tungsten functionalized silica nanoparticles (WSN) used in this study.

Table 1. Measured values of tungsten nanoparticle diameter (MSAP), dispersion, and surface area of hybrid nanoparticles, WSN.

Material	* $S_{BET} \pm 0.1$ m^2/g	* MSAP ± 0.1 nm	Tungsten Dispersion (%)
SiO$_2$	126.1	-	-
SiWNa1 350	122.3	1.6	26.1
SiWNa1 450	92.9	1.9	19.5
SiWNa1 650	101.1	2.6	16.5
SiWNa3 350	108.5	7.6	13.6
SiWNa3 450	93.5	8.6	10.8
SiWNa3 650	94.3	10.2	5.6
SiWNa5 350	94.7	9.5	5.6
SiWNa5 450	94.2	13.7	3.1
SiWNa5 650	93.7	15.4	2.9
SiW1 350	81.1	1.8	15.2
SiW1 450	79.6	3.4	12.6
SiW1 650	66.2	4.7	9.1

* Uncertainty is obtained by triplicate measurements.

2.2.4. Nanoparticles Characterization

The silica nanoparticles were characterized using dynamic light scattering technique (DLS) for hydrodynamic diameter by a nanoplus-3 from Micromeritics, USA. Characterization of functional groups on the nanoparticles and WSN surface was performed by Fourier transform infrared spectroscopy (FTIR) with an IRAffinity-1 FTIR spectrophotometer from Shimadzu, Japan. Determination of tungsten dispersion and the average size of crystal on silica nanoparticles or mean particle size of active phase (MSAP) was performed by H$_2$ pulse chemisorption with a Chembet 3000 (Quantachrome Instruments, Boynton Beach, FL, USA) with a high-sensitivity thermal conductivity detector. The procedure is detailed in other work [63]. Quantitative hydrogen pulses (10 µL) were injected until the surface was saturated, and W–H species were formed [64–66]. The surface area (S_{BET}) of catalysts were obtained by N$_2$ adsorption/desorption experiments in an Autosorb-1 from Quantachrome [67,68]. The S_{BET} was estimated based on the Brunauer−Emmet−Teller (BET) method which is detailed elsewhere [69]. X-ray photoelectron spectroscopy tests were performed for selected catalysts on a Specs X-ray photoelectronic spectrometer (NAP-XPS) with a PHOIBOS 150 1D-DLD analyzer, using a monochromatic source of Al-Kα (1486.7 eV, 13 kV, 100 W). Details of the experimental setup are found in a previous work [44].

2.2.5. Equilibrium Adsorption Isotherms

A stock solution of 2000 mg·L^{-1} was prepared by dissolving the extracted asphaltenes in toluene; later, model solutions were made ranging from 100 mg·L^{-1} to 2000 mg·L^{-1}. Batch adsorption experiments were carried out at 25 °C, adding the nanoparticles to the model solutions at a fixed nanoparticles-to-solution ratio of 100 mg to 10 mL [70]. The mixtures were stirred for 12 h at 300 rpm to ensure equilibrium; then, the WSN with the adsorbed asphaltenes were separated from the asphaltenes in solution by centrifugation. The absorbance of the supernatant was measured using a Genesys 10S UV–Vis spectrophotometer, taking the toluene as a blank. A calibration curve was previously constructed for a wavelength of 295 nm, and, in this way, determining the adsorbed amount of asphaltenes per nanoparticle area surface is determined by the mass balance of the analysis. The amount adsorbed q (mg·m^{-2}) was determined using Equation (1):

$$q = (C_0 - C_E)\frac{V}{A} \tag{1}$$

where C_0 (mg·L^{-1}) is the initial concentration of asphaltenes, C_E (mg·L^{-1}) is equilibrium concentrations in solution after adsorption, V (L) is volume of the solution, and A (m^2·g^{-1}) is the dry surface area of the employed material. The adsorption isotherms for the asphaltenes onto the nanoparticles were modeled using the solid–liquid equilibrium (SLE) model [38] (see Equations (S1) to (S3) in the support information).

2.2.6. Thermogravimetric Analysis

To evaluate the catalytic behavior of the materials, the thermal stability of the asphaltenes (adsorbate) in the presence and absence of the adsorbent was studied. Thermogravimetric tests were performed on asphaltenes, and nanoparticles obtained after the batch adsorption tests (previously dried) on a TGA Q50 from TA Instruments, Inc, New Castle, DE. The samples were dried for 12 h, and 5 mg of each one was taken for thermogravimetric analysis kept low to circumvent the diffusion limitations [71]. The samples were analyzed on wet combustion atmosphere from 30 °C to 600 °C at three different rates (5 °C·min^{-1}, 10 °C·min^{-1}, and 20 °C·min^{-1}) using a wet airflow (5%, volumetric fraction) rate constant 100 mL·min^{-1} throughout the experiment. Steam is generated in an evaporator (filled with deionized water) with a temperature controller, which fixes the vapor pressure based on the temperature set point. The wet airflow is obtained when the airflow stream is injected through the evaporator, reaching its saturation at the vapor pressure required [72]. For the adsorbents selected as the best catalysts, their capacity to produce in situ hydrogen and other calorific gases was analyzed via mass spectrometry using a mass spectrometer (Shimadzu GC-MS, Tokyo, Japan). Details of the setup are found in other works [28,73]. The components targeted for the analysis by single-ion monitoring in mass spectrometry were H$_2$ (2 g·mol^{-1}), CO (28 g·mol^{-1}), CO$_2$ (44 g·mol^{-1}), and LHC (C$_2$H$_4$, C$_2$H$_6$, CH$_4$). Reproducibility was ensured, realizing the experiments by triplicate. In addition, the effective activation energies were estimated by the method of Ozawa–Flynn–Wall (OFW). This methodology is extensively found in the literature and reported in previous reports [28,73], with good reproducibility (see Equations (S4)–(S7)).

3. Results and Discussion

3.1. Nanoparticle Characterization

The results obtained for the hydrodynamic diameter of synthesized SiO$_2$ nanoparticles are in the nanometer range with a mean value of 12.5 nm $\pm$ 2 nm. This size is suitable for application in oilfields because its size is smaller than pore throats of heavy oil reservoirs [74]. Table 1 shows the properties of the nanoparticles, BET surface area, tungsten dispersion, and average size of the tungsten nanoparticles in the supported catalyst. Each type of nanoparticle exhibited a different chemical nature.

Pulsed H_2 chemisorption determines the exposed metallic atoms at the surface, using H_2 as a molecule probe, which does not interact significantly with the support material (SiO_2), but forms a strong chemical bond to the surface metallic atoms causing the H_2 spillover and consequently its consumption. The W surface area and dispersion were calculated, assuming dissociative chemisorption of hydrogen with a stoichiometry of W–H of 1 [65,75]. Results of the tungsten mean particle size under the measurement of reduced particles for the studied samples are also shown in Table 1 and confirm the formation of tungsten nanoparticles (tungsten oxides) over the support surface. It can be observed that by increasing the calcination temperature, the obtained nanoparticles are bigger in size due to the thermally promoted particle growth. Meanwhile, the particle dispersion has an inverse trend: as the calcination temperature is increased, particle dispersion decreases. The tendency obtained for the variation of impregnation dosage used is similar; a greater quantity implies a crystal with larger size, and, in turn, lower dispersion. Hence, the formation of the tungsten oxide nanoparticles over the SiO_2 surface is strongly influenced by synthesis conditions.

The obtained S_{BET} values for the nanomaterials are also listed in Table 1. As expected, the sample prepared at 350 °C has the highest surface area of 122.3 $m^2 \cdot g^{-1}$. The values of the measured S_{BET} followed the order 350 °C > 450 °C > 650 °C and 1% > 3% > 5%, according to calcination temperature and impregnation dosage, respectively. As the temperature of calcination is raised, the surface area decreases [76]. It is well known that the temperature favors the atomic movements and, therefore, an increase of the crystallite size. Thus, a bigger size of the crystalline domain implies an increase of the particle dimension and a reduction of its surface area. In porous materials, it is also reported that the increase of the temperature can induce a collapse of the porous structure and a densification of the material. The behavior described in the reduction of the surface area is in agreement with the reported in other works [28,33].

XPS was used to investigate the oxidation states and chemical environment of W species on the surface of the as-synthesized catalysts; the results are shown in Figure 1. In an XPS survey spectra (see Figure S1) of selected catalysts, binding energies of the O_{1s} and Si_{2s} levels for all the catalysts agreed with the values obtained for silica (O_{1s} = 532.9 eV and Si_{1s} = 155.3 eV) [77]. The catalysts present significant signals at 531.3 eV and 285 eV, possibly due to the presence of hydroxyl groups and carbonate species or *C–C* bonds in carbon impurities (adventitious carbon) [78,79].

The W_{4f} HR-XPS core-level spectrum (Figure 1) reveals that the W_{4f} doublet (5/2 and 7/2) presents at least four different signals corresponding to different W species at the surface. From approximately 33.8 eV to 36.2 eV and from 36.2 eV to 40 eV represent the spin orbit splitting $W_{4f\,7/2}$ and $W_{4f\,5/2}$, respectively. Then, each of these regions was decomposed into two different signals, corresponding to different oxidation states or chemical environments of the tungsten superficial atoms. In general, the signals are displaced to higher energy with the increasing calcination temperature, indicating that the tungsten is surrounded by a high electronegative environment or is more oxidized when the temperature increases. W_{4f} electrons from WO_3 have binding energies at around 35.9 eV and 38.0 eV for 7/2 and 5/2 orbits, respectively [80–82]. As is shown in Figure 1a, another signal displaced to less binding energy is found in all W4f HR-XPS. These signals vary between 34.8 eV to 35.5 eV and 36.6 eV to 37.3 eV for 7/2 and 5/2 orbits, respectively. Generally, the spectrum of supported WO_3 is broader than massif WO_3 due to the interaction between the tungsten oxides and the support [83]. On another side, the broadening of the spectrum toward the high and low binding energy flack suggests that the supported tungsten is not fully oxidized, and possibly the surface contains small amounts of W_{5+} on the supported catalysts. The analysis of the high-resolution XPS for W_{4f} suggests that the surface of the tungsten nanoparticles contains a large quantity of defects which diminish with the increasing of the temperature. These defects cause a nonstoichiometry oxide by the apparition of oxygen vacancies $\left(V_O^2\right)$ at the surface and in the bulk as well. A nonstoichiometry oxide can be written as shown in Equation (2), where the missing charges can be balanced by a

reduction of the W cations. In the Supplementary Information is shown the whole process (in Kröger–Vink notation) of the vacancy formation and reduction of the cations inside of a tungsten oxide (Equation (S8)–(S10)). Thus, the changes in BE shown in W_{4f} high-resolution XPS (Figure 1) are associated with the oxygen vacancy formation and the cation reduction from 6+ to 5+, in accord with the BE values.
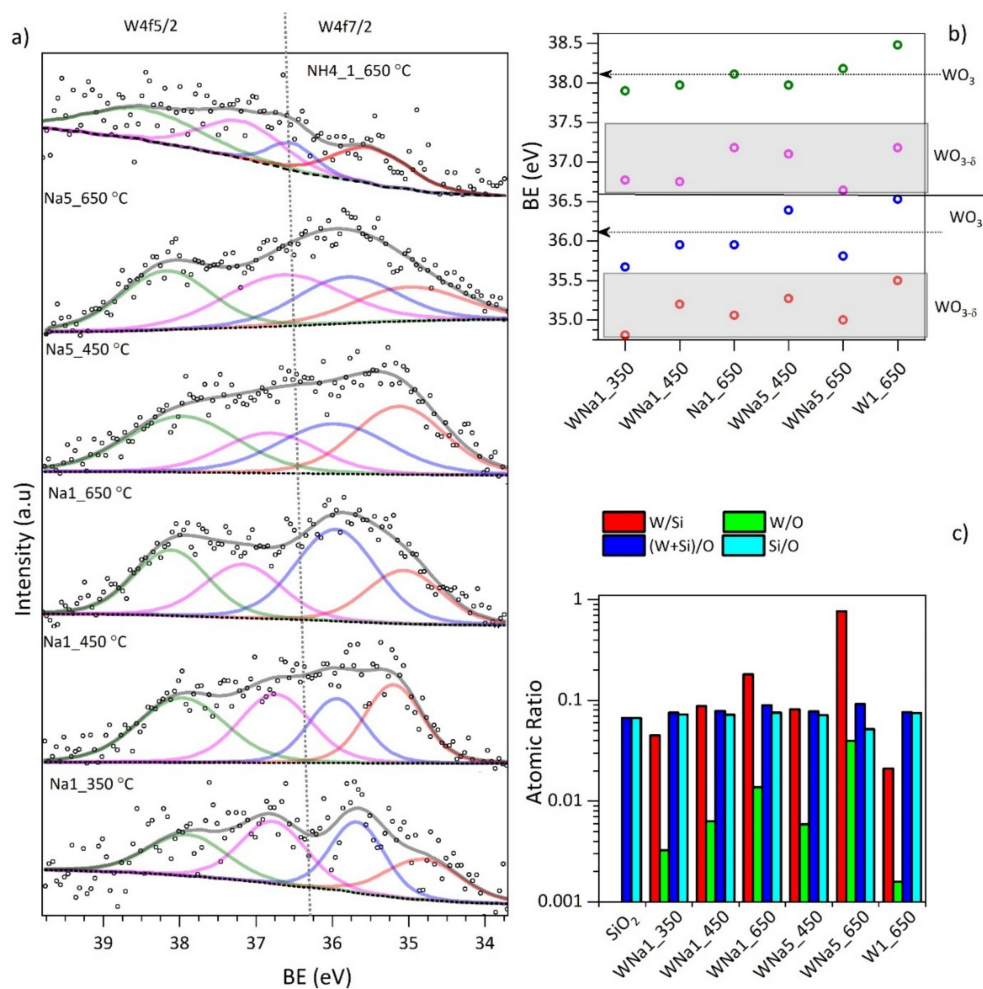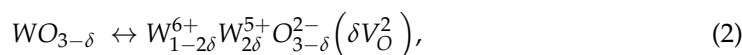
$$WO_{3-\delta} \leftrightarrow W^{6+}_{1-2\delta} W^{5+}_{2\delta} O^{2-}_{3-\delta} \left(\delta V^2_O \right), \tag{2}$$

Figure 1. (**a**) XPS high-resolution spectra of the W_{4f} doublet 4f7/2 and 4f5/2. (**b**) Binding energy of W surface species on selected nanoparticles. (**c**) Atomic ratio of each species in the selected WSN.

Different reports show that the tungsten oxides can produce oxygen vacancies, and that its quantity can be modulated though the heating temperature and the atmosphere as well [84–88]. These defects play an important role in the physicochemical properties, such as catalytic [89] and photocatalytic activity [85], quantum confinement [86], and ionic conductivity [85], among others.

The atomic ratio of surface elements is shown in Figure 1c; all the catalysts showed small changes of Si/O ratio whereas W/Si and W/O ratios were different between catalysts. Considering the ratio of W/O and (W)/Si, which indicated the surface dispersion and concentration of tungsten on a silica support, a direct relation is seen to calcination temperature, relatively greater than the impregnation dosage used on each one [77,89]

3.2. Asphaltene Adsorption Isotherms

Effect of Synthesis Conditions

Figure 2a–f shows the obtained adsorption isotherms of asphaltenes by SiWNa and SiW samples at 25 °C with the SLE model. For every sample, the sorption isotherms revealed an increase in the adsorbed asphaltene content as the asphaltene concentration increased. It should be noted that SHS adsorbed more asphaltenes than SiO_2 nanoparticles for all asphaltene concentrations. The difference was more noticeable at higher concentrations ($C_E > 200$ mg·L^{-1}), which agrees with previous results [28,36,46–50]. These results agree with literature reports for the adsorption of different asphaltene types onto different solid surfaces [36,37,42,43,73]. The adsorption isotherms follow a type Ib behavior according to the IUPAC classification [87], indicating that there is a strong affinity between the n-C_7 asphaltenes and the synthesized materials [31,90].
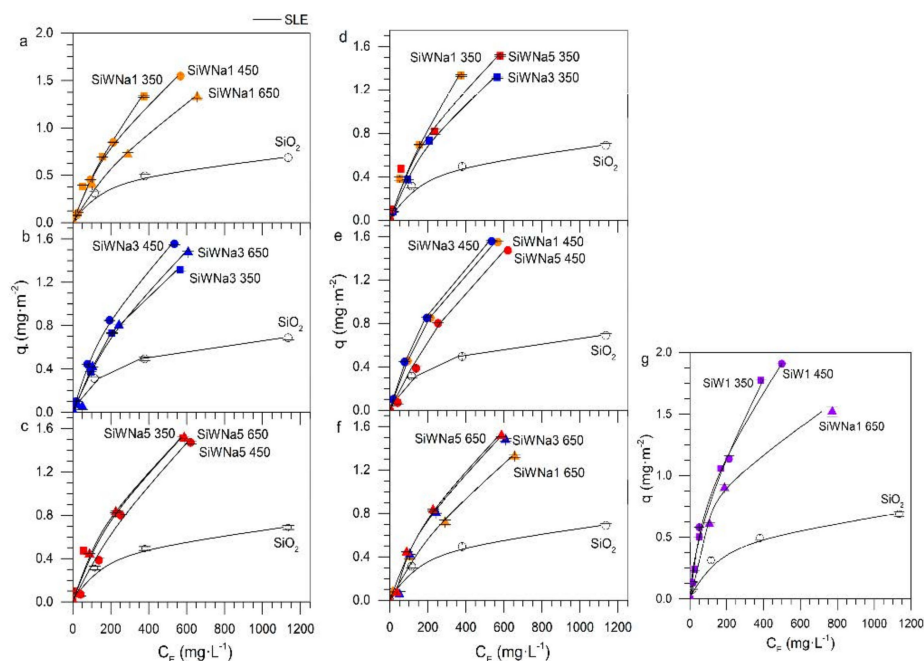

Figure 2. Adsorption isotherms of n-C_7 asphaltenes onto supported nanoparticles: Effect of calcination temperature at the same impregnation dosage; (**a**–**c**) effect of calcination temperature at the same impregnation dosage; effect of impregnation dosage at the same calcination temperature (**d**–**f**); effect of precursor (**g**). Nanoparticle dose, 10 g·L^{-1}; agitation speed, 200 rpm; T, 25 °C. The symbols are experimental data, and the solid lines are from the SLE model (see Equation (2)).

On another side, considering the acidic character of tungsten oxide, this behavior suggests the basicity of the asphaltenes in addition the presence of heteroatoms such as nitrogen and oxygen in the asphaltene molecules, which favor the interaction with the nanoparticle surface [91,92]. It could be observed in Figure 2a–f that there is a trend on the adsorptive capacity highly influenced by synthesis conditions of WSN following the general orders SiWNa1 > SiWNa3 > SiWNa5 > SiO_2 and SiWNa350 > SiWNa 450 > SiWNa 650 > SiO_2. The SLE model parameters are enlisted in Table 2. Additionally, the adsorption affinity, represented by the reciprocal of H value, increases for lower tungsten impregnation dosage, except for the virgin support. The same trend can be observed by the degree of asphaltene self-association on active sites, which is represented by K. This parameter decreases with the increase in impregnation dosage, and the lowest value is obtained for the virgin support. Conversely, the inverse trend can be observed for the q_m parameter. From values of q_m and the H parameter, it can be observed that the functionalized nanoparticles show more affinity and adsorption capacity than the support. In addition, lower values of

the *K* parameter suggest that the inclusion of tungsten oxide allows the inhibition of the adsorbate self-association.

Table 2. SLE model parameters of asphaltenes adsorption by studied nanoparticles at 25 °C with the effect of calcination temperature at the same impregnation dosage, the effect of impregnation dosage at the same calcination temperature, and effect of the precursor.

Material	H (mg·g^{-1})	$K \times 10^{-4}$ (g/g)	q_m (g·g^{-1})	R^2	χ^2
Si	2.27	6.61	1.29	0.99	0.49
SiWNa1 350	0.76	1.73	3.21	0.99	0.19
SiWNa1 450	1.90	1.89	4.41	0.99	0.62
SiWNa1 650	2.60	2.02	4.80	0.99	0.48
SiWNa3 350	1.90	2.03	4.37	0.99	0.19
SiWNa3 450	2.07	4.35	4.95	0.99	0.62
SiWNa3 650	2.18	5.37	4.66	0.99	0.48
SiWNa5 350	1.75	1.19	4.20	0.99	1.00
SiWNa5 450	2.25	1.46	4.78	0.99	1.25
SiWNa5 650	2.67	2.40	5.51	0.99	0.18
SiW1 350	1.24	1.64	6.02	0.99	0.46
SiW1 450	1.58	1.84	5.95	0.99	0.50
SiW1 650	1.75	2.30	3.14	0.99	0.14

Van der Waals forces, polar, and acid–base (Lewis and/or Brønsted) interactions seem to be the dominant forces that contribute to the adsorption of the asphaltenes onto tungsten oxide and/or salt surfaces [93]. Previous studies concluded that the adsorption of asphaltenes over silica is due to the chemisorption of asphaltenes on the silica silanol groups [94]. On the other hand, acid sites are responsible for adsorption of basic molecules that contain heteroatoms [91,92]. Due to the low acidity of silica, the presence of tungsten oxide generates the formation of Brønsted acid sites and the increase of Lewis acid sites [95], increasing interactions with the basic sites of the asphaltenes, or heteroatoms N, O, and S, which makes the interaction stronger and consequently increases the number of asphaltenes adsorbed.

Figure 2g shows the obtained adsorption isotherms of asphaltenes by SiW at 25 °C with the SLE model. The asphaltene uptake is enhanced after functionalizing the SiO$_2$ with the trend SiW1 > SiW3 > SiW5 > Si and SiW 350 > SiW 450 > SiW 650 > SiO$_2$. Figure S2 compares the obtained adsorption isotherms of asphaltenes by SiW1 350 and SiWNa1 350 at 25 °C with the SLE model. In this case, the amount adsorbed of asphaltenes is higher than SiWNa nanoparticles; in addition, SiW nanoparticles showed a similar adsorption affinity than SiWNa. These differences could be due to electronic effects and different interactions between the active phase and the support (as seen in XPS analysis) that influence the selectivity for different functional groups or heteroatoms in *n*-C$_7$ asphaltene molecules [43].

Figure 3 presents the trends of the *H* and *K* parameters of the SLE model. Figure 3a shows the trends for functionalized nanoparticles from sodium tungstate at different dosage calcination temperatures. Here, in the parameter *H*, as the calcination temperature increases, the value increases, which suggests that the higher the calcination temperature, the lower the affinity. On the other hand, parameter *K* shows that as the calcination temperature increases for the same dosage, the self-association of the asphaltenes increases.

During XPS analysis, a direct relationship between calcination temperature and W/O and W/Si ratios was demonstrated, which indicated that the surface dispersion and concentration of tungsten on a silica support depends on the calcination temperature used. In addition, the tungsten nanoparticles contain a large quantity of defects that are diminishing with the increasing calcination temperature. All these properties affect the adsorptive behavior of nanoparticles and their ability to inhibit the self-association degree of asphaltenes on their surfaces.
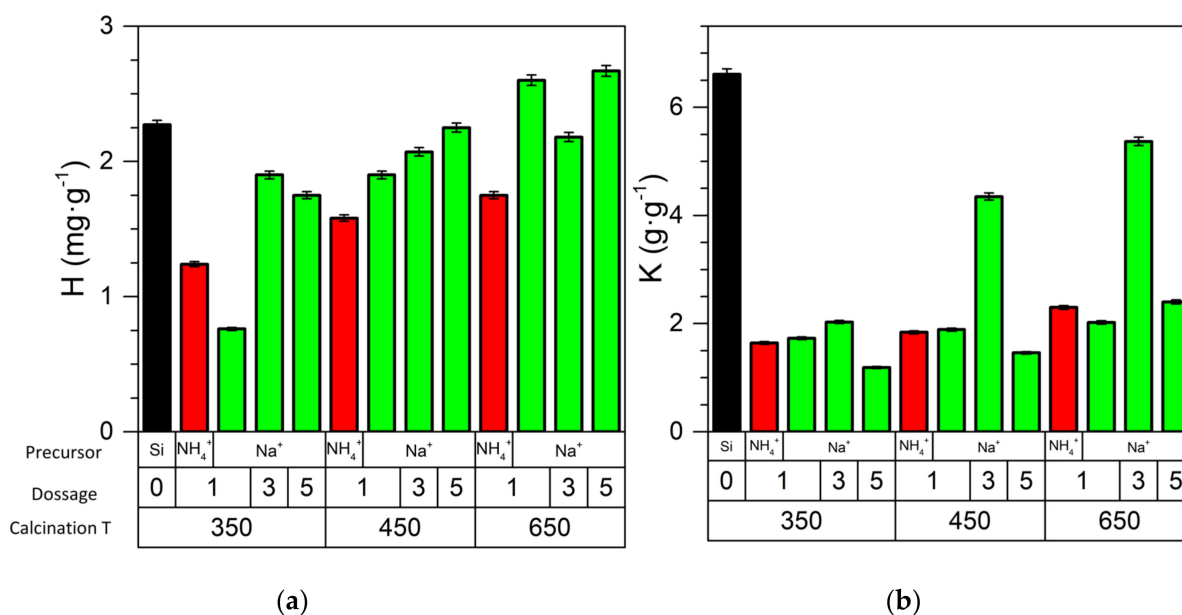
Figure 3. Trends for *K* and *H* parameters of the adjustment model of the adsorption isotherms (**a**) with nanoparticles functionalized from sodium tungstate at different calcination rates and temperatures, and (**b**) with functionalized nanoparticles from ammonium tungstate and sodium tungstate at 1% (mass fraction) and different calcination temperatures.

Figure 4b shows that, likewise for nanoparticles functionalized from ammonium tungstate, the affinity value increases as the calcination temperature increases, which suggests a lower affinity. Regarding the parameter *K*, there is a slight increase in the value, which suggests a greater self-association of the asphaltenes as the calcination temperature increases.

Asphaltene adsorption over the surface of the nanoparticles depends on factors such as asphaltene concentration on the medium, affinity interactions, and availability of active sites [38,61]. However, at medium and high uptake [38,43], due to their self-associated tendency asphaltenes, molecules will form aggregates around the high-energy sites until saturation [61,96]. On another side, the asphaltenes adsorption is subject to the adsorbent surface selectivity to the aromatic part of the asphaltenes or heteroatoms present in their structure, generating different adsorption orientations (perpendicular, parallel, or flatways) [61]. Following this order of ideas, with the functionalization of the nanoparticles, selectivity is induced, and the conditions used during material synthesis could influence the amount of active sites available for asphaltene adsorption; at the same time, the obtained results suggest that these conditions affect the characteristics of supported metal oxide, such as dispersion and active phase size, influence the adsorptive capacity of support, and enhance its affinity for asphaltenes [97]. It is important to remark that the adsorption capacity seems to be enhanced after functionalization at a lower dosage.
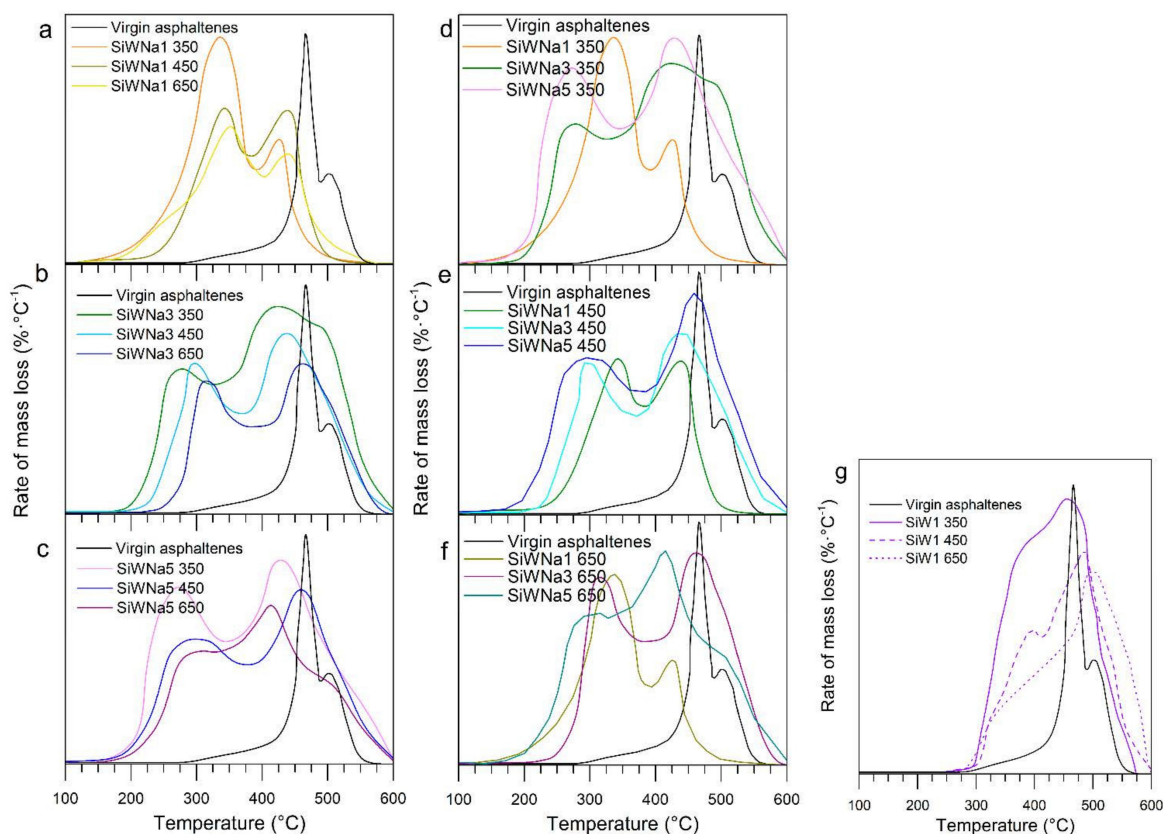
Figure 4. The plot of the rate of mass loss as a function of temperature in the steam/air atmosphere and conversion for asphaltenes in the presence of nanoparticles: (**a–c**) effect of calcination temperature at the same impregnation dosage; effect of impregnation dosage at the same calcination temperature (**d–f**); effect of precursor (**g**). Amount adsorbed = 0.2 mg·m^{-2}; air flow rate = 100 mL·min^{-1}; H$_2$O (**g**) flow rate = 6.30 mL·min^{-1}.

3.3. Catalytic Steam Decomposition of n-C$_7$ Asphaltenes

3.3.1. Mass Loss Analysis

The tests were carried out in a wet air atmosphere for a specific asphaltene loading of 0.20 mg·m^{-2}. Figure 4 shows the rate of mass loss for the virgin n-C$_7$ asphaltenes in the absence and presence of SiWNa. Figure 4a–c compares the presence of nanoparticles using the same impregnation dosage, and Figure 4e–f compare the presence of nanoparticles using the same calcination temperature during nanoparticles synthesis. As seen for virgin n-C$_7$ asphaltenes, the reaction has an onset approximately at 325 °C, with a maximum peak at 465 °C and an offset near to 574 °C. In this case, the presence of silica nanoparticles did not prove to be effective in reducing the decomposition temperature of asphaltenes. Figure 5 shows that, generally, the curve for asphaltenes rate of mass loss in the presence of WSN shifts to the left, confirming that decomposition occurs at a lower temperature. For the best scenarios evaluated with the WSN (SiWNa1 350, SiWNa450, and SiWNa650), the maximum peak of mass loss rate was reduced from 465 °C to 325 °C. In previous reports, the support (SiO$_2$) was evaluated without any functionalization, showing that it reduces the temperature of transformation of asphaltenes a bit under different atmospheres, including inert or thermal cracking [73], steam gasification, and air (or combustion [28]). In this case, the presence and absence of water into the stream was also evaluated, showing that the decomposition profile remains unchanged. However, a change in the produced gases was observed and more gasification products were found (H$_2$, CO, and CH$_4$). These products will be analyzed in the following section.
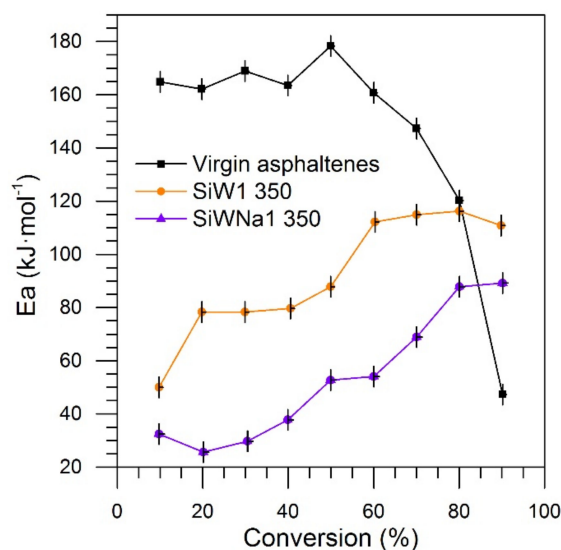
Figure 5. Effective activation energies calculated by OFW method as a function of the % conversion for catalytic decomposition of virgin asphaltenes in the presence and absence of selected WSN with both precursor salts at 1% (in mass fraction).

The conversion of n-C_7 asphaltenes to gaseous products can be associated with their partial oxidation, pyrolysis, and gasification [16]. Steam presence in the decomposition of asphaltenes as carbonaceous source implies different reactions, such as water–gas shift reaction and methanation [43]. The catalytic decomposition of asphaltenes in the presence of WSN can be divided into two reaction regions, LTR (low-temperature reaction, before 400 °C) and HTR (high-temperature reaction, between 400 °C and 600 °C). Initially, reactions on the breakdown of alkyl chains take place and the dissociation of weak bonds (S–C and N–C) [93,98], followed by the opening of polycyclic aromatic hydrocarbons and radical or addition reactions that can form heavier compounds (these compounds could be larger from the starting species turning into coke) [51,99]. With the increase in the temperature, there are still some reactions attributed to the gasification and oxidation of resultant compounds produced by free radicals that were not stabilized and due to addition reactions [42]. In the catalytic decomposition process, irrespective of the atmosphere (wet air), the first step includes the oxidation and low-temperature gasification of the asphaltenes. Hence, the volatile content is released, and the remaining condensed aromatic sheets subsequently react. Later, the oxygen present reacts with condensed aromatic sheets oxidizing first outer layers and, at relatively higher temperatures, the internal layers [93].

The inclusion of WSN reduces the temperature of asphaltene consumption. In all cases, two main peaks are observed, one on LTR and another on HTR. It is inferred that the first peak corresponds to the breaking of weakest bonds of asphaltenes and the second, to the decomposition of more stable structures, such as aromatic condensed rings. The presence of H_2O can enhance the process of asphaltenes decomposition, due to the reaction of gaseous H_2 or O_2 previously adsorbed such as water over the nanoparticle matrix and active sites with adsorbed molecules that would be cracked, and free radicals formed which are highly reactive and can aid to decompose other molecules, i.e., raw asphaltenes. According to the results obtained, the surface properties and the catalytic activity of the nanoparticles affect how asphaltenes and water are adsorbed over the active sites, leading to a highly efficient process in energetic terms [43]. In the studied cases, the first peak temperature is considerably reduced by nanoparticles at approximately 100 °C and for the WSN that shows the best catalytic activity, SiWNa1 350. Changing the precursor does not show significant catalytic activity (Figure 4g), a factor that could be attributed to poor dispersion, acidity, affinity, or the big size of the active phase. It is considered that acid sites influence the asphaltenes conversion [100]. Isomerization reactions occur on the Brønsted acid sites

of the WO_3/SiO_2 catalysts, and studies have concluded that by poisoning the surface acid sites with small amounts of alkali elements, such as Na, K, Rb, and Cs, branched metathesis products were decreased, that is, isomerization was reduced, obtaining a greater degree of asphaltenes consumption [101–103].

Regarding the SLE parameters, it can also be noticed a direct relation between the catalytic effect of the synthesized materials with the affinity for asphaltene adsorption and the degree of self-association. With lower values of H and K parameters of the SLE model, the catalytic behavior of the surface is higher. The asphaltene auto-association degree would impact the catalytic activity of the nanoparticle blocking this one, due to that the formation of large aggregates could block some active sites [61]. The highest tungsten oxide dispersion and the lowest active phase showed a higher reduction of decomposition temperature.

3.3.2. Estimation of the Effective Activation Energies

Another way to validate the catalytic activity of the nanoparticles consists of the estimation of the effective activation energies through the isoconversional OFW methodology. For this case, the nanoparticle that demonstrated the highest efficiency in hydrogen production and reduction of asphaltene decomposition temperature was selected to analyze the effective activation energy behavior (that is, SiWNa1 350). For comparative purposes, the nanoparticle was selected with the same metal dosage, calcined at the same temperature, but with different precursors, that is, SiW1 350.

Figure 5 shows the estimated effective activation energies as a function of the degree of conversion. For virgin n-C_7 asphaltenes, the value of Ea decreases as the conversion increases, which agrees well with previous reports under different reaction atmospheres [28,72,95]. Conversely, for the decomposition n-C_7 asphaltenes in the presence of SiWNa1 350 and SiW1 350 nanoparticles, the opposite trend is observed. It is worth remarking that, in all cases for conversion < 80%, the effective activation energy is shown to be lower compared with the virgin n-C_7 asphaltene; this again confirms the catalytic activity of the nanoparticles. For the catalytic asphaltene decomposition, the activation energy increases with the degree of conversion, suggesting that the catalytic decomposition consists of a complex mechanism that involves multiple steps [42,104]. SiWNa1 350 displayed the lowest activation energy throughout the process, suggesting that this sample is more catalytically active toward SiW1 350. The reduction of the effective activation energy is of primary importance to enhance the wet in-situ combustion, as a more efficient heat consumption can be ensured and could lead to higher oil recovery with upgraded characteristics.

As discussed above, the temperature of calcination affects the size of particles and the surface chemical environment. For lower temperatures, a small particle, high dispersion, and more quantity of defects are found. Though the XPS analysis, lower binding energies were found when the calcination temperature was set at 350 °C, showing that the W cations were in the lowest oxidation state (on average). Therefore, for these catalysts (350 °C), it is expected to find the largest quantity of surface defects, such as oxygen vacancies and reduced tungsten cations. These couples of punctual defects $\left(V_O^2 \cdots W_W^{x'} \right)$ constitute a redox or basic–acid site that promotes the adsorption and activation of the different reactants, such as water, oxygen, and hydrocarbons, favoring the reaction kinetics (see Figure S3).

3.3.3. Analysis of the Gaseous Products Evolved during Catalytic Decomposition Process

During the asphaltenes decomposition though wet air gasification, different gases such as CO, CH_4, H_2, light hydrocarbons (LHC), and CO_2 can be released. In this study, the releases gases during virgin asphaltene and catalytic steam gasification with SiWNa1 350 were analyzed using mass spectrometry. The SiWNa1 350 sample was selected based on catalytic results reported in previous sections. The experimental nonisothermal heating at 10 °C·min^{-1} was considered, and the results of the gaseous products are shown in Figure 6. As expected, the gaseous mixture was composed of CO_2, CH_4, CO, C_2H_2, C_2H_4, C_6H_6,

and H_2. The gases C_2H_2, C_2H_4, and C_6H_6 will be referred to as light hydrocarbons (LHC). Some traces of other gases were evidenced in different temperature intervals, but they were neglected (selective distribution < 1.0% vol).
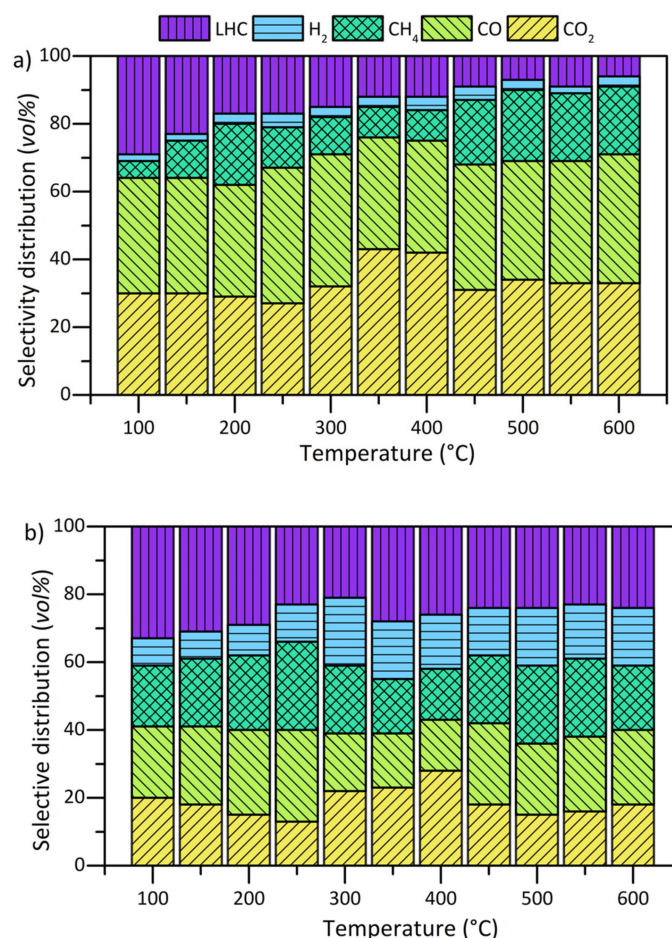

Figure 6. Selectivity distribution of light gases produced from the nonisothermal conversion of asphaltenes (**a**) without and (**b**) with SiWNa 350 nanoparticles between 100 and 600 °C. Air flow rate = 100 mL·min^{-1}; $H_2O_{(g)}$ flow rate = 6.30 mL·min^{-1}; asphaltene load = 0.0002 mmol·m^{-2}; heating rate = 10 °C·min^{-1}.

Panel a shows the evolution of the different gases with temperature change for virgin asphaltene decomposition. The gas mixture was composed mainly for CO and CO_2. The CO evolved increased with temperature because of the reverse Boudouard reaction. The CO_2 is produced by different mechanisms, including the transformation of ketones and other oxygenated groups in the asphaltene chemical structure. The produced LHC was evidenced during all the temperature range evaluated. However, at lower temperatures (<200 °C), the higher release of them was noted because of the breaking and decomposition of aliphatic chains and low-molecular-weight hydrocarbons. Finally, H_2 release was poor in the noncatalyzed sample because these heavy fractions follow other reaction mechanisms that prioritize the production of other gases, such as CO_2 and CO [29].

The results of the catalyzed sample are shown in panel b. The results show an increase in LHC, CH_4, and H_2 during the wide range of temperature. At lower temperatures (<250 °C), the LHC production is slightly higher than the uncatalyzed system because of the loss of aliphatic chains and low-molecular-weight hydrocarbons. In the catalyzed scenario, the LHC mixture is composed mainly of C_2H_4 (>60%vol), a highly calorific gas; while in the noncatalyzed scenario, this gas was produced to a lesser extent (<30%vol).

On the other hand, CO_2 production decreased between 200–300 °C, whereas CO and CH_4 increased in the same range. CO_2 reacts with carbon atoms to produce CO while CH_4 is released by the breaking of methyl, methylene, and other short aliphatic chains. Then, between 300 and 400 °C, a drop in CO and a slight increase in CO_2 and H_2 is observed. This behavior can be attributed to the occurrence of water–gas-shift reaction [105]. In addition, methane-reforming reactions appear to occur in the same range of temperature as a reduction of the CH_4 content in the gas mixture. It is worth mentioning that hydrogen released was higher than the noncatalyzed system in all the temperature range. It can be produced by the reaction of C in asphaltenes and $H_2O_{(g)}$ molecules. The higher hydrogen content was 20%vol between 300 and 400 °C.

In the thermic process, reactions of total or partial combustion are common (formation of CO); in the presence of steam, the methanation (formation of CH_4) and steam reforming are common [106]. The increase of CH_4 production in the presence of nanoparticles with respect to virgin asphaltenes suggests an increment in methanation reactions promoted by the action of nanoparticles; at the same time, in addition to the combustion reaction by the presence of O_2, part of the formed CH_4 and the reaction in water present in steam form CO. These reactions are aligned with the upgrading process in the reservoir as lighter compounds would lead to viscosity reduction and API gravity increase.

4. Conclusions

Asphaltene adsorption and subsequent catalytic decomposition on functionalized silica nanoparticles with tungsten oxides were studied using model solutions on batch adsorption experiments and TGA/MS system for evaluating thermocatalytic properties in a steam/air atmosphere. Dispersion and medium active phase size of supported oxides were shown to be essential factors in the catalytic and adsorptive behavior of nanoparticles. Sodium tungstate and tungsten oxide supported nanocatalysts were compared, and the results showed a similar adsorptive capacity but a marked difference in catalytic behavior.

XPS analysis demonstrated a direct relationship between calcination temperature and W/O and W/Si ratios, which indicated the surface dispersion and concentration of tungsten on a silica support, depending on the calcination temperature used. In addition, the tungsten nanoparticles contain a large quantity of defects that are diminishing with the increasing calcination temperature. All these properties affect the adsorptive behavior of nanoparticles and their ability to inhibit the self-association degree of asphaltenes on their surfaces.

The catalytic results show that synthesized nanoparticles reduce asphaltene decomposition temperature. In addition, synthesis parameters, such as temperature and impregnation dosage, play an important role in the catalytic activity of the materials due to the different WOX–support interactions. The mixture released during the catalyzed asphaltene decomposition in the wet air atmosphere reveals an increase in light hydrocarbons, methane, and hydrogen content. Hydrogen production was prioritized between 300 and 400 °C, where the reduction of CO, CH_4 and the increase in CO_2 content similarly occurs, associated with water–gas-shift and methane-reforming reactions, respectively.

The results obtained in this research project suggest that the SiO_2 nanoparticles functionalized with tungsten oxides (WSN) can be used as catalysts for the in situ upgrading of heavy crude oil during wet in situ combustion

Institutional Review Board Statement: Not applicable.

Informed Consent Statement: Not applicable.

Data Availability Statement: Not applicable.

Conflicts of Interest: The authors declare no conflict of interest.

Nomenclature

API	American Petroleum Institute
C_0	Initial concentration of asphaltenes
C_E	Equilibrium concentrations in solution after adsorption
DLS	Dynamic light scattering
EHO	Extra-heavy oil
HO	Heavy oil
H	Henry's law constant
HTR	High-temperature reaction
K	Self-association degree
LTR	Low-temperature reaction
LHC	Light hydrocarbons
MSAP	Mean particle size of active phase
OFW	Ozawa–Flynn–Wall
PAH	Polyaromatic hydrocarbons
q_m	Maximum adsorbed amount
TEOR	Thermal enhanced oil recovery
TEO	Transition element oxides
TGA	Thermogravimetric analysis
SLE	Solid–liquid equilibrium
S_{BET} (m^2)	BET surface area
SSS	Sodium silicate solution
WSN	Tungsten functionalized silica nanoparticles
XPS	X-ray photoelectron spectroscopy
R	Universal gas constant
T	Absolute temperature
E_α	Activation energy

References

1. Zaid, A.M.; Al-Dousari, M.M. Forces Driving Oil and Gas Demand Cycles. In Proceedings of the International Petroleum Technology Conference, Dubai, United Arab Emirates, 4–8 December 2007.
2. Alboudwarej, H.; Felix, J.J.; Taylor, S.; Badry, R.; Bremner, C.; Brough, B.; Skeates, C.; Baker, A.; Palmer, D.; Pattison, K. La importancia del petróleo pesado. *Oilfield Rev.* **2006**, *18*, 38–58.
3. Medina, O.E.; Gallego, J.; Rodríguez, E.; Franco, C.A.; Cortés, F.B. Effect of pressure on the oxidation kinetics of Asphaltenes. *Energy Fuels* **2019**, *33*, 10734–10744. [CrossRef]
4. Medina, O.E.; Olmos, C.; Lopera, S.H.; Cortés, F.B.; Franco, C.A. Nanotechnology applied to thermal enhanced oil recovery processes: A review. *Energies* **2019**, *12*, 4671. [CrossRef]

5. Mitra-Kirtley, S.; Mullins, O.C. Sulfur chemical moieties in carbonaceous materials. In *Asphaltenes, Heavy Oils, and Petroleomics*; Springer: New York, NY, USA, 2007; pp. 157–188.

6. Tissot, B.P.; Welte, D.H. *Petroleum Formation and Occurrence*; Springer Science & Business Media: Berlin/Heidelberg, Germany, 2013.

7. Groenzin, H.; Mullins, O.C. Asphaltene molecular size and structure. *J. Phys. Chem. A* **1999**, *103*, 11237–11245. [CrossRef]

8. Mullins, O.C. The asphaltenes. *Annu. Rev. Anal. Chem.* **2011**, *4*, 393–418. [CrossRef]

9. Strausz, O.P.; Lown, E.M. *The Chemistry of Alberta Oil Sands, Bitumens and Heavy Oils*; Alberta Energy Research Institute: Calgary, AB, Canada, 2003.

10. Yudin, I.; Nikolaenko, G.; Gorodetskii, E.; Kosov, V.; Melikyan, V.; Markhashov, E.; Frot, D.; Briolant, Y. Mechanisms of asphaltene aggregation in toluene–heptane mixtures. *J. Pet. Sci. Eng.* **1998**, *20*, 297–301. [CrossRef]

11. Murgich, J.; Abanero, J.A.; Strausz, O.P. Molecular recognition in aggregates formed by asphaltene and resin molecules from the Athabasca oil sand. *Energy Fuels* **1999**, *13*, 278–286. [CrossRef]

12. Demirbas, A. Deposition and flocculation of asphaltenes from crude oils. *Pet. Sci. Technol.* **2016**, *34*, 6–11. [CrossRef]

13. Medina, O.E.; Gallego, J.; Cespedes, S.; Nassar, N.N.; Montoya, T.; Corteś, F.B.; Franco, C.A. Effect of pressure on thermo-oxidative reactions of saturates, aromatics, and resins (S-Ar-R) from extra-heavy crude oil. *Fuel* **2021**, *311*, 122596. [CrossRef]

14. Adams, J.J. Asphaltene adsorption, a literature review. *Energy Fuels* **2014**, *28*, 2831–2856. [CrossRef]

15. Zahedi, G.; Fazlali, A.; Hosseini, S.; Pazuki, G.; Sheikhattar, L. Prediction of asphaltene precipitation in crude oil. *J. Pet. Sci. Eng.* **2009**, *68*, 218–222. [CrossRef]

16. Nassar, N.N.; Hassan, A.; Pereira-Almao, P. Application of nanotechnology for heavy oil upgrading: Catalytic steam gasification/cracking of asphaltenes. *Energy Fuels* **2011**, *25*, 1566–1570. [CrossRef]

17. Medina, O.E.; Gallego, J.; Redondo, J.D.; Cortés, F.B.; Franco, C.A. Effect of pressure on the thermo-oxidative behavior of saturates, aromatics, and resins (S-Ar-R) mixtures. *Fuel* **2021**, 122787. [CrossRef]

18. Allenson, S.J.; Walsh, M.A. A novel way to treat asphaltene deposition problems found in oil production. In Proceedings of the International Symposium on Oilfield Chemistry, Houston, TX, USA, 18 February 1997.

19. Chang, J.; Ivory, J. Steam-Air Injection Process. In Proceedings of the SPE Canada Heavy Oil Technical Conference, Calgary, AB, Canada, 8 June 2016.

20. Kokal, S.L.; Sayegh, S.G. Asphaltenes: The cholesterol of petroleum. In Proceedings of the Middle East Oil Show, Bahrain, Saudi Arabia, 15 March 1997.

21. Saniere, A.; Hénaut, I.; Argillier, J. Pipeline transportation of heavy oils, a strategic, economic and technological challenge. *Oil Gas Sci. Technol.* **2004**, *59*, 455–466. [CrossRef]

22. Medina, O.E.; Gallego, J.; Nassar, N.N.; Acevedo, S.A.; Cortés, F.B.; Franco, C.A. Thermo-Oxidative Decomposition Behaviors of Different Sources of n-C7 Asphaltenes at High-Pressure Conditions. *Energy Fuels* **2020**, *34*, 8740. [CrossRef]

23. Bagci, A.S. Wet forward combustion for heavy oil recovery. *Energy Sources Part A* **2006**, *28*, 221–232. [CrossRef]

24. Lapene, A.; Castanier, L.M.; Debenest, G.; Quintard, M.Y.; Kamp, A.M.; Corre, B. Effects of Water on Kinetics of Wet In-Situ Combustion. In Proceedings of the SPE Western Regional Meeting, San Jose, CA, USA, 1 January 2009; p. 12.

25. Ward, G.D.; Ward, C.E. Insitu Wet Combustion Process for Recovery of Heavy Oils. Google Patents US4691773A, 8 September 1987.

26. Sarathi, P.S. *In-Situ Combustion Handbook—Principles and Practices*; National Petroleum Technology Office: Sawfa, Saudi Arabia, 1999.

27. Greaves, M.; Young, T.; El-Usta, S.; Rathbone, R.; Ren, S.; Xia, T. Air injection into light and medium heavy oil reservoirs: Combustion tube studies on West of Shetlands Clair oil and light Australian oil. *Chem. Eng. Res. Des.* **2000**, *78*, 721–730. [CrossRef]

28. Franco, C.A.; Montoya, T.; Nassar, N.N.; Pereira-Almao, P.; Cortés, F.B. Adsorption and Subsequent Oxidation of Colombian Asphaltenes onto Nickel and/or Palladium Oxide Supported on Fumed Silica Nanoparticles. *Energy Fuels* **2013**, *27*, 7336–7347. [CrossRef]

29. Medina, O.E.; Gallego, J.; Acevedo, S.; Riazi, M.; Ocampo-Pérez, R.; Cortés, F.B.; Franco, C.A. Catalytic Conversion of n-C7 Asphaltenes and Resins II into Hydrogen Using CeO2-Based Nanocatalysts. *Nanomaterials* **2021**, *11*, 1301. [CrossRef]

30. Cardona, L.; Medina, O.E.; Céspedes, S.; Lopera, S.H.; Cortés, F.B.; Franco, C.A. Effect of Steam Quality on Extra-Heavy Crude Oil Upgrading and Oil Recovery Assisted with PdO and NiO-Functionalized Al$_2$O$_3$ Nanoparticles. *Processes* **2021**, *9*, 1009. [CrossRef]

31. Medina, O.E.; Gallego, J.; Pérez-Cadenas, A.F.; Carrasco-Marín, F.; Cortés, F.B.; Franco, C.A. Insights into the Morphology Effect of Ceria on the Catalytic Performance of NiO–PdO/CeO$_2$ Nanoparticles for Thermo-oxidation of n-C7 Asphaltenes under Isothermal Heating at Different Pressures. *Energy Fuels* **2021**, *35*, 18170–18184. [CrossRef]

32. Mateus, L.; Moreno-Castilla, C.; López-Ramón, M.V.; Cortés, F.B.; Álvarez, M.Á.; Medina, O.E.; Franco, C.A.; Yebra-Rodríguez, Á. Physicochemical characteristics of calcined MnFe$_2$O$_4$ solid nanospheres and their catalytic activity to oxidize para-nitrophenol with peroxymonosulfate and n-C7 asphaltenes with air. *J. Environ. Manag.* **2021**, *281*, 111871. [CrossRef]

33. Arias-Madrid, D.; Medina, O.E.; Gallego, J.; Acevedo, S.; Correa-Espinal, A.A.; Cortés, F.B.; Franco, C.A. NiO, Fe$_2$O$_3$, and MoO$_3$ Supported over SiO$_2$ Nanocatalysts for Asphaltene Adsorption and Catalytic Decomposition: Optimization through a Simplex–Centroid Mixture Design of Experiments. *Catalysts* **2020**, *10*, 569. [CrossRef]

34. Hashemi, R.; Nassar, N.N.; Almao, P.P. Nanoparticle technology for heavy oil in-situ upgrading and recovery enhancement: Opportunities and challenges. *Appl. Energy* **2014**, *133*, 374–387. [CrossRef]

35. Hosseinpour, N.; Mortazavi, Y.; Bahramian, A.; Khodatars, L.; Khodadadi, A.A. Enhanced pyrolysis and oxidation of asphaltenes adsorbed onto transition metal oxides nanoparticles towards advanced in-situ combustion EOR processes by nanotechnology. *Appl. Catal. A Gen.* **2014**, *477*, 159–171. [CrossRef]

36. Nassar, N.N.; Hassan, A.; Pereira-Almao, P. Metal Oxide Nanoparticles for Asphaltene Adsorption and Oxidation. *Energy Fuels* **2011**, *25*, 1017–1023. [CrossRef]

37. Cortés, F.B.; Chejne, F.; Carrasco-Marín, F.; Pérez-Cadenas, A.F.; Moreno-Castilla, C. Water sorption on silica-and zeolite-supported hygroscopic salts for cooling system applications. *Energy Convers. Manag.* **2012**, *53*, 219–223. [CrossRef]

38. Montoya, T.; Coral, D.; Franco, C.A.; Nassar, N.N.; Cortés, F.B. A novel solid–liquid equilibrium model for describing the adsorption of associating asphaltene molecules onto solid surfaces based on the "chemical theory". *Energy Fuels* **2014**, *28*, 4963–4975. [CrossRef]

39. Krishnamoorti, R. Extracting the benefits of nanotechnology for the oil industry. *J. Pet. Technol.* **2006**, *58*, 24–26. [CrossRef]

40. Medina, O.E.; Galeano-Caro, D.; Ocampo-Pérez, R.; Perez-Cadenas, A.F.; Carrasco-Marín, F.; Franco, C.A.; Cortés, F.B. Development of a monolithic carbon xerogel-metal composite for crude oil removal from oil in-saltwater emulsions: Evaluation of reuse cycles. *Microporous Mesoporous Mater.* **2021**, *327*, 111424. [CrossRef]

41. Medina, O.E.; Galeano-Caro, D.; Castelo-Quibén, J.; Ocampo-Pérez, R.; Perez-Cadenas, A.F.; Carrasco-Marín, F.; Franco, C.A.; Cortés, F.B. Monolithic carbon xerogels-metal composites for crude oil removal from oil in-saltwater emulsions and subsequent regeneration through oxidation process: Composites synthesis, adsorption studies, and oil decomposition experiments. *Microporous Mesoporous Mater.* **2021**, *319*, 111039. [CrossRef]

42. Franco, C.A.; Montoya, T.; Nassar, N.N.; Cortés, F.B. NiO nd PdO supported on fumed silica nanoparticles for adsorption and catalytic steam gasification of colombian c7asphaltenes. In *Handbook on Oil Production Research*; Nova Science Hauppauge: New York, NY, USA, 2014.

43. Nassar, N.N.; Franco, C.A.; Montoya, T.; Cortés, F.B.; Hassan, A. Effect of oxide support on Ni–Pd bimetallic nanocatalysts for steam gasification of n-C7 asphaltenes. *Fuel* **2015**, *156*, 110–120. [CrossRef]

44. Medina, O.E.; Gallego, J.; Restrepo, L.G.; Cortés, F.B.; Franco, C.A. Influence of the Ce4+/Ce3+ Redox-Couple on the Cyclic Regeneration for Adsorptive and Catalytic Performance of NiO-PdO/CeO2±δ Nanoparticles for n-C7 Asphaltene Steam Gasification. *Nanomaterials* **2019**, *9*, 734. [CrossRef] [PubMed]

45. Medina, O.E.; Caro-Vélez, C.; Gallego, J.; Cortés, F.B.; Lopera, S.H.; Franco, C.A. Upgrading of Extra-Heavy Crude Oils by Dispersed Injection of NiO–PdO/CeO2±δ Nanocatalyst-Based Nanofluids in the Steam. *Nanomaterials* **2019**, *9*, 1755. [CrossRef]

46. Franco-Ariza, C.A.; Guzmán-Calle, J.D.; Cortés, F.B. Adsorption and catalytic oxidation of asphaltenes in fumed silica nanoparticles: Effect of the surface acidity. *Dyna* **2016**, *83*, 171. [CrossRef]

47. Nassar, N.N.; Hassan, A.; Carbognani, L.; Lopez-Linares, F.; Pereira-Almao, P. Iron oxide nanoparticles for rapid adsorption and enhanced catalytic oxidation of thermally cracked asphaltenes. *Fuel* **2012**, *95*, 257–262. [CrossRef]

48. Nassar, N.N.; Hassan, A.; Pereira-Almao, P. Comparative oxidation of adsorbed asphaltenes onto transition metal oxide nanoparticles. *Colloids Surf. A: Physicochem. Eng. Asp.* **2011**, *384*, 145–149. [CrossRef]

49. Nassar, N.N.; Hassan, A.; Pereira-Almao, P. Effect of surface acidity and basicity of aluminas on asphaltene adsorption and oxidation. *J. Colloid Interface Sci.* **2011**, *360*, 233–238. [CrossRef]

50. Nassar, N.N.; Hassan, A.; Pereira-Almao, P. Effect of the particle size on asphaltene adsorption and catalytic oxidation onto alumina particles. *Energy Fuels* **2011**, *25*, 3961–3965. [CrossRef]

51. Nassar, N.N.; Hassan, A.; Pereira-Almao, P. Thermogravimetric studies on catalytic effect of metal oxide nanoparticles on asphaltene pyrolysis under inert conditions. *J. Therm. Anal. Calorim.* **2012**, *110*, 1327–1332. [CrossRef]

52. Barton, D.G.; Soled, S.L.; Iglesia, E. Solid acid catalysts based on supported tungsten oxides. *Top. Catal.* **1998**, *6*, 87–99. [CrossRef]

53. Speight, J.G. *Fouling in Refineries*; Gulf Professional Publishing: Houston, TX, USA, 2015.

54. J Spivey, J.; Dooley, K.M.; Han, Y.-F.; Meunier, F.; Tshentu, Z.R.; Dai, W.-L.; Jin, R.; Efstathiou, A.; Meunier, F.; Coppens, M.-O.; et al. *Catalysis*; Royal Society of Chemistry: Picadilly, UK, 2016; Volume 28.

55. Kung, H.H. *Transition Metal Oxides: Surface Chemistry and Catalysis*; Elsevier: Amsterdam, The Netherlands, 1989; Volume 45.

56. Wasmi, B.A.; Al-Amiery, A.A.; Kadhum, A.A.H.; Mohamad, A.B. Novel approach: Tungsten oxide nanoparticle as a catalyst for malonic acid ester synthesis via ozonolysis. *J. Nanomater.* **2014**, *2014*, 2. [CrossRef]

57. Barre, L.; Espinat, D.; Rosenberg, E.; Scarsella, M. Colloidal structure of heavy crudes and asphaltene soltutions. *Rev. De L'institut Français Du Pétrole* **1997**, *52*, 161–175. [CrossRef]

58. ASTM. *D5236-13 Standard Test Method for Distillation of Heavy Hydrocarbon Mixtures (Vacuum Potstill Method). Annual Book of ASTM Standards*; ASTM International: West Conshohocken, PA, USA, 2013.

59. ASTM. *D2892 Standard Test Method for Distillation of Crude Petroleum (15-Theoretical Plate Column). Annual Book of ASTM Standards*; ASTM International: West Conshohocken, PA, USA, 2016.

60. Franco, C.; Patiño, E.; Benjumea, P.; Ruiz, M.A.; Cortés, F.B. Kinetic and thermodynamic equilibrium of asphaltenes sorption onto nanoparticles of nickel oxide supported on nanoparticulated alumina. *Fuel* **2013**, *105*, 408–414. [CrossRef]

61. Franco, C.A.; Nassar, N.N.; Montoya, T.; Ruíz, M.A.; Cortés, F.B. Influence of asphaltene aggregation on the adsorption and catalytic behavior of nanoparticles. *Energy Fuels* **2015**, *29*, 1610–1621. [CrossRef]

62. Vert, M.; Hellwich, K.-H.; Hess, M.; Hodge, P.; Kubisa, P.; Rinaudo, M.; Schué, F. Terminology for biorelated polymers and applications (IUPAC Recommendations 2012). *Pure Appl. Chem.* **2012**, *84*, 377–410. [CrossRef]

63. Medina, O.E.; Gallego, J.; Arias-Madrid, D.; Cortés, F.B.; Franco, C.A. Optimization of the load of transition metal oxides (Fe$_2$O$_3$, Co$_3$O$_4$, NiO and/or PdO) onto CeO$_2$ nanoparticles in catalytic steam decomposition of n-C7 asphaltenes at low temperatures. *Nanomaterials* **2019**, *9*, 401. [CrossRef]

64. Diao, W.; Tengco, J.M.M.; Regalbuto, J.R.; Monnier, J.R. Preparation and characterization of Pt–Ru bimetallic catalysts synthesized by electroless deposition methods. *ACS Catal.* **2015**, *5*, 5123–5134. [CrossRef]

65. Geyer, R.; Hunold, J.; Keck, M.; Kraak, P.; Pachulski, A.; Schödel, R. Methods for determining the metal crystallite size of Ni supported catalysts. *Chem. Ing. Tech.* **2012**, *84*, 160–164. [CrossRef]

66. Shastri, A.G.; Schwank, J. Metal dispersion of bimetallic catalysts via stepwise chemisorption and surface titration: I. Ru_AuSiO$_2$. *J. Catal.* **1985**, *95*, 271–283. [CrossRef]

67. Socrates, G. *Infrared and Raman Characteristic Group Frequencies: Tables and Charts*; John Wiley & Sons: Hoboken, NJ, USA, 2004.

68. Yao, H.; Dai, Q.; You, Z. Fourier Transform Infrared Spectroscopy characterization of aging-related properties of original and nano-modified asphalt binders. *Constr. Build. Mater.* **2015**, *101*, 1078–1087. [CrossRef]

69. Leofanti, G.; Padovan, M.; Tozzola, G.; Venturelli, B. Surface area and pore texture of catalysts. *Catal. Today* **1998**, *41*, 207–219. [CrossRef]

70. Guzmán, J.D.; Betancur, S.; Carrasco-Marín, F.; Franco, C.A.; Nassar, N.N.; Cortés, F.B. Importance of the Adsorption Method Used for Obtaining the Nanoparticle Dosage for Asphaltene-Related Treatments. *Energy Fuels* **2016**, *30*, 2052–2059. [CrossRef]

71. Giraldo, J.; Nassar, N.N.; Benjumea, P.; Pereira-Almao, P.; Cortés, F.B. Modeling and prediction of asphaltene adsorption isotherms using Polanyi's modified theory. *Energy Fuels* **2013**, *27*, 2908–2914. [CrossRef]

72. Cortés, F.B.; Chejne, F.; Carrasco-Marín, F.; Moreno-Castilla, C.; Pérez-Cadenas, A.F. Water adsorption on zeolite 13X: Comparison of the two methods based on mass spectrometry and thermogravimetry. *Adsorption* **2010**, *16*, 141–146. [CrossRef]

73. Montoya, T.; Argel, B.L.; Nassar, N.N.; Franco, C.A.; Cortés, F.B. Kinetics and mechanisms of the catalytic thermal cracking of asphaltenes adsorbed on supported nanoparticles. *Pet. Sci.* **2016**, *13*, 561–571. [CrossRef]

74. Franco Ariza, C.A. *Synthesis and Application of Supported Metallic and Multi-Metallic Oxides Nanoparticles for In-Situ Upgrading and Inhibition of Formation Damage*; Universidad Nacional de Colombia: Bogota, Columbia, 2015.

75. López, D.; Giraldo, L.J.; Salazar, J.P.; Zapata, D.M.; Ortega, D.C.; Franco, C.A.; Cortés, F.B. Metal Oxide Nanoparticles Supported on Macro-Mesoporous Aluminosilicates for Catalytic Steam Gasification of Heavy Oil Fractions for On-Site Upgrading. *Catalysts* **2017**, *7*, 319. [CrossRef]

76. Chen, Y.-F.; Lee, C.-Y.; Yeng, M.-Y.; Chiu, H.-T. The effect of calcination temperature on the crystallinity of TiO2 nanopowders. *J. Cryst. Growth* **2003**, *247*, 363–370. [CrossRef]

77. Colque, S.; Payen, E.; Grange, P. Novel preparation of highly dispersed tungsten oxide on silica. *J. Mater. Chem.* **1994**, *4*, 1343–1348. [CrossRef]

78. Elkins, T.W.; Hagelin-Weaver, H.E. Characterization of Mn–Na$_2$WO$_4$/SiO$_2$ and Mn–Na$_2$WO$_4$/MgO catalysts for the oxidative coupling of methane. *Appl. Catal. A: Gen.* **2015**, *497*, 96–106. [CrossRef]

79. Salmaoui, S.; Sediri, F.; Gharbi, N.; Perruchot, C.; Jouini, M. Hexagonal hydrated tungsten oxide nanomaterials: Hydrothermal synthesis and electrochemical properties. *Electrochim. Acta* **2013**, *108*, 634–643. [CrossRef]

80. Terohid, S.A.A.; Heidari, S.; Jafari, A.; Asgary, S. Effect of growth time on structural, morphological and electrical properties of tungsten oxide nanowire. *Appl. Phys. A* **2018**, *124*, 567. [CrossRef]

81. Biesinger, M.C. X-ray Photoelectron Spectroscopy (XPS) Reference Pages. Available online: http://www.xpsfitting.com/ (accessed on 1 May 2020).

82. Agilent Scientific Instruments, Thermo Scientific XPS Simplified. Available online: https://xpssimplified.com/ (accessed on 1 May 2020).

83. Susanti, D.; Diputra, A.A.G.P.; Tananta, L.; Purwaningsih, H.; Kusuma, G.E.; Wang, C.; Shih, S.; Huang, Y. WO$_3$ nanomaterials synthesized via a sol-gel method and calcination for use as a CO gas sensor. *Front. Chem. Sci. Eng.* **2014**, *8*, 179–187. [CrossRef]

84. Bursill, L.A. Structure of small defects in nonstoichiometric WO$_{3-x}$. *J. Solid State Chem.* **1983**, *48*, 256–271. [CrossRef]

85. Fukushi, D.; Sasaki, A.; Hirabayashi, H.; Kitano, M. Effect of oxygen vacancy in tungsten oxide on the photocatalytic activity for decomposition of organic materials in the gas phase. *Microelectron. Reliab.* **2017**, *79*, 1–4. [CrossRef]

86. Tanaka, D.; Oaki, Y.; Imai, H. Enhanced photocatalytic activity of quantum-confined tungsten trioxide nanoparticles in mesoporous silica. *Chem. Commun.* **2010**, *46*, 5286–5288. [CrossRef]

87. Thommes, M.; Kaneko, K.; Neimark, A.V.; Olivier, J.P.; Rodriguez-Reinoso, F.; Rouquerol, J.; Sing, K.S.W. Physisorption of gases, with special reference to the evaluation of surface area and pore size distribution (IUPAC Technical Report). *Pure Appl. Chem.* **2015**, *87*, 1051. [CrossRef]

88. Zhang, H.; Feng, M.; Liu, F.; Liu, L.; Chen, H.; Gao, H.; Li, J. Structures and defects of WO$_{3-x}$ nanorods grown by in-situ heating tungsten filament. *Chem. Phys. Lett.* **2004**, *389*, 337–341. [CrossRef]

89. Gayapan, K.; Sripinun, S.; Panpranot, J.; Praserthdam, P.; Assabumrungrat, S. Effect of pretreatment atmosphere of WO$_X$/SiO$_2$ catalysts on metathesis of ethylene and 2-butene to propylene. *RSC Adv.* **2018**, *8*, 11693–11704. [CrossRef]

90. Medina, O.E.; Gallego, J.; Olmos, C.M.; Chen, X.; Cortés, F.B.; Franco, C.A. Effect of multifunctional nanocatalysts on n-C7 asphaltene adsorption and subsequent oxidation under high-pressure conditions. *Energy Fuels* **2020**, *34*, 6261–6278. [CrossRef]

91. Ramirez-Corredores, M.M. *The Science and Technology of Unconventional Oils: Finding Refining Opportunities*; Academic Press: Cambridge, MA, USA, 2017.

92. Zimmer, A.K.; Becker, C.; Chambliss, C.K. Exploiting metal oxide nanoparticle selectivity in asphaltenes for identification of pyridyl-containing molecules. *Energy Fuels* **2013**, *27*, 4574–4580. [CrossRef]

93. Hosseinpour, N.; Khodadadi, A.A.; Bahramian, A.; Mortazavi, Y. Asphaltene adsorption onto acidic/basic metal oxide nanoparticles toward in situ upgrading of reservoir oils by nanotechnology. *Langmuir* **2013**, *29*, 14135–14146. [CrossRef]

94. Fritschy, G.; Papirer, E. Interactions between a bitumen, its components and model fillers. *Fuel* **1978**, *57*, 701–704. [CrossRef]

95. Andreini, A.; Mol, J.C. Activity of supported tungsten oxide catalysts for the metathesis of propene. *J. Chem. Soc. Faraday Trans. 1: Phys. Chem. Condens. Phases* **1985**, *81*, 1705–1714. [CrossRef]

96. Dudášová, D.; Simon, S.; Hemmingsen, P.V.; Sjöblom, J. Study of asphaltenes adsorption onto different minerals and clays: Part 1. Experimental adsorption with UV depletion detection. *Colloids Surf. A: Physicochem. Eng. Asp.* **2008**, *317*, 1–9. [CrossRef]

97. Contreras, J.L.; Fuentes, G.A. Sintering of Supported Metal Catalysts. In *Sintering-Methods and Products*; InTech: London, UK, 2012.

98. Siddiqui, M.N. Catalytic pyrolysis of Arab Heavy residue and effects on the chemistry of asphaltene. *J. Anal. Appl. Pyrolysis* **2010**, *89*, 278–285. [CrossRef]

99. Hamedi Shokrlu, Y.; Babadagli, T. In-situ upgrading of heavy oil/bitumen during steam injection by use of metal nanoparticles: A study on in-situ catalysis and catalyst transportation. *SPE Reserv. Eval. Eng.* **2013**, *16*, 333–344. [CrossRef]

100. Breysse, M.; Furimsky, E.; Kasztelan, S.; Lacroix, M.; Perot, G. Hydrogen activation by transition metal sulfides. *Catal. Rev.* **2002**, *44*, 651–735. [CrossRef]

101. Kawai, T.; Goto, H.; Yamazaki, Y.; Ishikawa, T. Metathesis of n-alkenes over a CsNO3-Re2O7-Al2O3 catalyst. *J. Mol. Catal.* **1988**, *46*, 157–172. [CrossRef]

102. Spamer, A.; Dube, T.; Moodley, D.; Van Schalkwyk, C.; Botha, J. The reduction of isomerisation activity on a WO3/SiO2 metathesis catalyst. *Appl. Catal. A: Gen.* **2003**, *255*, 153–167. [CrossRef]

103. Van Roosmalen, A.; Mol, J. Active centers for the metathesis and isomerization of alkenes on tungsten-oxide/silica catalysts. *J. Catal.* **1982**, *78*, 17–23. [CrossRef]

104. Nassar, N.N.; Hassan, A.; Vitale, G. Comparing kinetics and mechanism of adsorption and thermo-oxidative decomposition of Athabasca asphaltenes onto TiO2, ZrO2, and CeO2 nanoparticles. *Appl. Catal. A: Gen.* **2014**, *484*, 161–171. [CrossRef]

105. Gradisher, L.; Dutcher, B.; Fan, M. Catalytic hydrogen production from fossil fuels via the water gas shift reaction. *Applied Energy* **2015**, *139*, 335–349. [CrossRef]

106. Kök, M.V.; Pamir, M.R. Pyrolysis and combustion studies of fossil fuels by thermal analysis methods. *J. Anal. Appl. Pyrolysis* **1995**, *35*, 145–156. [CrossRef]